ARTICLE OPEN

Stabilizing electromagnons in CuO under pressure

M. Verseils[1✉], P. Hemme[2], D. Bounoua[3], R. Cervasio[1], J-B. Brubach[1], S. Houver[2], Y. Gallais[2], A. Sacuto[2], D. Colson[4], T. Iijima[5], M. Mochizuki[5], P. Roy[1] and M. Cazayous[2]

Electromagnons (Electroactive spin wave excitations) could prove to be decisive in information technologies but they remain fragile quantum objects, mainly existing at low temperatures. Any future technological application requires overcoming these two limitations. By means of synchrotron radiation infrared spectroscopy performed in the THz energy range and under hydrostatic pressure, we tracked the electromagnon in the cupric oxide CuO, despite its very low absorption intensity. We demonstrate how a low pressure of 3.3 GPa strongly increases the strength of the electromagnon and expands its existence to a large temperature range enhanced by 40 K. Accordingly, these two combined effects make the electromagnon of CuO under pressure a more ductile quantum object. Numerical simulations based on an extended Heisenberg model were combined to the Monte-Carlo technique and spin dynamics to account for the magnetic phase diagram of CuO. They enable to simulate the absorbance response of the CuO electromagnons in the THz range.

npj Quantum Materials (2023)8:11 ; https://doi.org/10.1038/s41535-023-00542-1

INTRODUCTION

Spin wave-based technologies (magnonics), in which spin waves (SW) are vectors for high-speed transmission and information processing at the nanometer scale initially relied on engineered media called magnonic crystals[1–3]. These crystals consist of a spatial periodic modulation of magnetic materials that were successfully developed for magnon transistors, phase shifters, or for spin wave logic gates[4]. Up to now, such SW are excited by dynamic magnetic fields generated by microwave currents. However, this method loses a lot of efficiency at the nanoscale due to parasitic couplings as the dimensions of the system decrease. Another perspective then emerged with the use of more versatile spin waves that an electric field could shape and guide on demand[5]. Such electroactive SW called electromagnons is the next step on the horizon for spin wave-based technologies. The main downside is that electromagnons are found only in a few compounds at room temperature and are weak quantum objects. Among these materials, CuO offers the possibility of driving such excitations to room temperature under pressure[6,7]. CuO crystallizes with the monoclinic C2/c space group and belongs to the type-II multiferroics. It undergoes, on cooling, a first magnetic transition at $T_N = 230$ K to a polar incommensurate antiferromagnetic spin-spiral phase labeled AF2 with a propagation vector $\mathbf{k} = (0.506;\ 0;\ 0.483)$[8,9]. Below 213 K the spin-spiral is locked-in towards a non-polar commensurate magnetic phase called AF1 (see Fig. 2)[10–12]. Jones et al.[13] observed an electromagnon (EM) in the multiferroic phase (AF2) using THz time-domain spectroscopy. EM could be excited with the electric field of light ($\mathbf{E}^{\omega}$) only along [101] and was measured ~20 cm^{-1} (0.6 THz) with a large width of ~30 cm^{-1} (0.9 THz). To account for these measurements, ab initio calculations based on SW dynamics[14] predicted two types of electromagnons associated with two different interactions. A first EM induced by the Dzyaloshinkii-Moriya (DM) is expected around 24 cm^{-1} (0.72 THz). A second EM due to exchange-striction interaction was predicted at 104 cm^{-1} (3.12 THz). In addition, X. Rocquefelte et al.[6] further predicted that CuO should exhibit multiferroic properties at room temperature under hydrostatic pressure as supported by recent dielectric constant measurements[7].

RESULTS

Infrared spectroscopy absorption measurements

Temperature dependence synchrotron radiation infrared spectroscopy measurements were performed in the THz energy range and in the transmission configuration, with polarized electric field of incident light $\mathbf{E}^{\omega}\|[101]$ of mm-thick CuO single crystal (0P-CuO, see Methods). High-pressure absorbance spectra were measured in a Diamond anvil cell (DAC) (see photo of the sample in Fig. 1) connected to the experimental low-temperature micro-focusing setup represented in Fig. 1 on 60 μm-thick single-crystal (HP-CuO, see Methods). The trade-off between sample size, achievable pressure, and detectable signal intensity allowed us to investigate four pressure values: 0.3, 1, 2, and 3.3 GPa as a function of temperature.

Figure 1 a and Fig. 1b–d show the relative absorbance spectra with $\mathbf{E}^{\omega}\|[101]$ measured outside the DAC on the 0P-CuO single crystal and inside the DAC on the HP-CuO sample, respectively see Methods). For each pressure, the high-temperature transmission spectra (250 K), collected in the paramagnetic (PM) phase was used as a reference for the calculation of the low T absorbance spectra. The data are expressed in terms of relative absorbance but can be interpreted as an "absolute" absorbance in this energy range since no absorption is observed from the sample at 250 K (meaning no EM, phonons, or other excitations at high temperatures in this energy range). We reported in supplementary Fig. 1 the relative absorbance obtained in the two perpendicular configurations (namely with $\mathbf{E}^{\omega}\|[10\bar{1}]$ and $\mathbf{E}^{\omega}\|[010]$). It confirms the absence of excitations in these channels.

At zero pressure (panel a), three absorption bands are observed with maximum intensities ~208 K. The first band at low energy is

[1]Synchrotron SOLEIL, L'orme des Merisiers, départementale 128, 91190 Saint-Aubin, France. [2]Laboratoire Matériaux et Phénomènes Quantiques, Université Paris Cité, CNRS, 10 rue Alice Domon et Léonie Duquet, 75205 Paris Cedex 13, France. [3]Université Paris-Saclay, CNRS-CEA,Laboratoire Léon Brillouin, 91191 Gif-sur-Yvette, France. [4]Service de Physique de l'Etat Condensé, CEA Saclay, IRAMIS, SPEC (CNRS URA 2464), F-91191 Gif sur Yvette, France. [5]Department of Applied Physics, Waseda University, Shinjuku-ku Tokyo 169-8555, Japan. ✉email: marine.verseils@synchrotron-soleil.fr

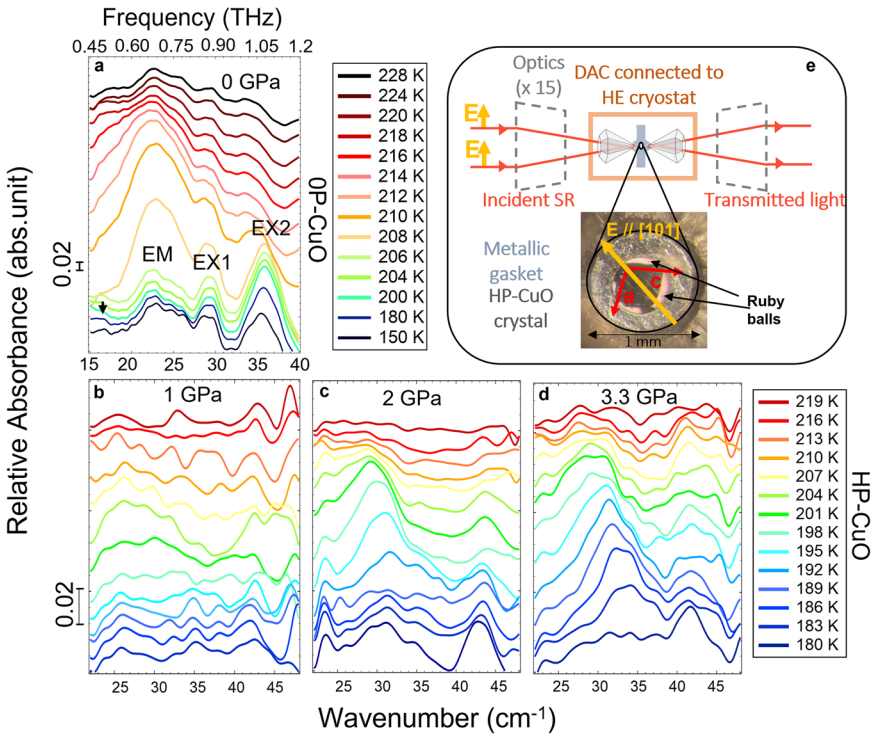

Fig. 1 THz absorbance of CuO electromagnons excited with E^{ω}||[101] under hydrostatic pressure. a Relative absorbance spectra of a mm-thick CuO sample (0P-CuO) measured for several temperatures at zero pressure. **b–d** Relative absorbance spectra measured for several temperatures and pressures on a 60 μm-thick sample placed inside a pressure cell (HP-CuO). The reference spectra used to calculate the absorbance are the transmission spectrum measured at high temperature (250 K) in the same conditions of pressure and alignment. The spectra are shifted in the vertical direction, but the relative intensities of absorbance are preserved, as represented by the 0.02 absorbance unit bar on bottom left corner of each graph. The spectra obtained at 0.3 GPa are reported in the supplementary Fig. 2. **e** Represents a schematic of the experiment with an image of the HP-CuO sample in the pressure cell and the orientation of its axes. The scale bar represents 1mm.

centered at 24 cm^{-1} (0.72 THz) and can thus be attributed to the already-known EM[13]. Two other excitations at 28 cm^{-1} (0.84 THz) and 36 cm^{-1} (1.08 THz) (labeled EX1 and EX2, respectively) are further revealed thanks to the high resolution of our set-up compared to the previous study[13] (these two excitations are probably hidden in the large right-hand tail of the EM peak in the measurement of Jones et al.[13]).

According to the thickness ratio between the two 0P-CuO and HP-CuO samples (~17, see Methods) used at zero and high pressure, we estimate the absorption band of EM to be less than 0.02 absorbance unit for the spectra obtained on the HP-CuO sample inside the DAC, which is close to the Signal/Noise ratio. Indeed, for the lowest pressure series (0.3 GPa, supplementary Fig. 2), the bands are hardly distinguishable. It is worth noting that the measurement of such excitations with very low absorption intensity (ten times smaller than phonons) on such thin sample (<100 μm suitable for high-pressure measurements) is very challenging. However, very interestingly, when the pressure is increased, the absorbance increases and the bands become visible (Fig. 1a–d). Thus, for pressure values higher than 0.3 GPa, two absorption bands are distinctly observed, corresponding to the aforementioned EM and EX2 excitations. EX1 instead is observed as the high-energy shoulder of the EM band. The intensity of the EM bands is enhanced by a factor 7 rising from 0.01 absorbance unit at 0.3 GPa to 0.07 absorbance unit at 3.3 GPa as illustrated in supplementary Fig. 4.

Temperature dependence at zero pressure

To unravel the behavior of the three excitations, we precisely studied their temperature dependence at zero pressure. The spectra obtained outside the DAC on the OP-CuO sample exhibit strong and well-resolved absorption bands (~0.4 absorbance unit) allowing their fitting to three Lorentzians on top of a linear background. We calculated the spectral weight of each mode, i.e., the area (integrated absorbance) of each peak, and reported the corresponding temperature dependence in Fig. 2. Below 120 K, there is no excitation and the areas are dominated by a background level. In the AF1 phase, between 120 K and 206 K, the area of the EM peak remains equal to this background value while the values for EX1 and EX2 increase linearly and reach their maxima at $T = 208$ K when the sample enters in the AF2 phase. Just above 208 K, the integrated absorbance of EM increases abruptly while the ones of EX1 and EX2 collapse. The integrated area of EM reaches its maximum value at 212 K, corresponding to the middle of the AF2 phase, and decreases at higher temperatures to recover the background level at 220 K, when CuO becomes paramagnetic (PM). These results evidence a spectral weight transfer from EX1 and EX2 to EM at the boundary of the AF1 and AF2 phases. Note that the frequencies of the three modes also shows anomalies at the AF1 to AF2 transition. In supplementary Fig. 3 one can observe an abrupt change in these frequencies at $T_{N1} = 208$ K. The origin of the EX1 and EX2 excitations is discussed below. Notice that, the transition temperature reported here corresponds to temperature of appearance and disappearance of the EM and not to the exact temperature of AF2 transition. This, added to an experimental systematic error due to the position of the sensor not directly touching the sample, explains the slight differences with the temperatures reported in literature.

Temperature dependence under high-pressure

For the absorbance spectra obtained at high-pressure, it was not possible to resolve the contribution of the different excitations so

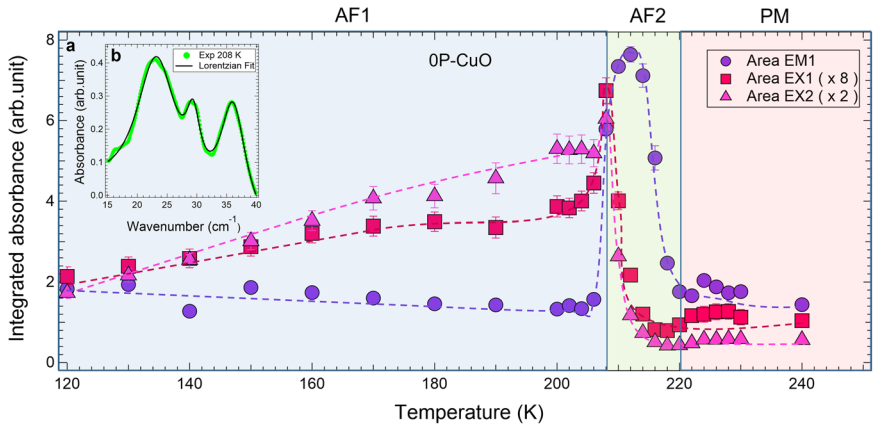

Fig. 2 Temperature dependence of the integrated electromagnon absorbance. a Integrated absorbance of the three excitations EM, EX1 and EX2 obtained from fitting the absorbance spectra of the 0P-CuO sample outside DAC, and as a function of temperature with $\mathbf{E}^{\omega}\|[101]$. The absolute values of the integrated absorbance of EX1 and EX2 were arbitrary multiplied by 8 and 2, respectively, in order to appear in the same scale as the values of the integrated absorbance of EM. **b** Example of Lorentzian fit on the spectrum at 208 K from Fig. 1a. For each point, error bar obtained from the fitting procedure is represented and visible if bigger than the point-size.

we calculated for each spectrum the integral between 20 and 50 cm^{-1} (0.6–1.5 THz). As discussed in the previous section, the EM excitation is a direct signature of the multiferroic (AF2) phase and represents the main contribution in this phase. The contribution of the EX1 and EX2 excitations will be treated as a background level. The integrated absorbance is an indicator of the electric-dipole activity of EM. On the upper panel of Fig. 3, we have reported a colormap of the integrated absorbance as a function of wavenumber and temperature. It clearly shows the increase of the spectral weight with pressure. For each temperature and for each pressure series, the value of the integrated absorbance is reported in the lower panel of Fig. 3. As discussed before, the background (gray in Fig. 2) due to EX1 and EX2 is high just before the appearance of EM and then decreases with T. Figure 3 shows several behaviors: (i) the EM activity increases with the pressure in agreement with the observation made on the spectra of Fig. 1. (ii) the maximum of the EM activity shifts to the low temperatures when pressure is increased (iii) its range of existence extends down to low and high temperatures when pressure is increased. On the basis of this last observation, we can identify the temperatures of appearance and disappearance of the EM excitation, on top of the background.

These results are summarized in the inset of Fig. 3, in the form of a P-T phase diagram. The existing temperature range of EM expands down to 178 K and up to 234 K at 3.3 GPa. By extrapolating our results, we expect that the EM electromagnon would be stabilized at room temperature around 10 GPa.

Numerical simulations

We also have performed numerical simulations using a method combining the Monte–Carlo technique and spin-dynamics simulations. We employ a classical Heisenberg model to describe the spin system in CuO, in which the biquadratic-interaction term (B_{biq}) is incorporated in addition to the symmetric ($\mathbf{S}\cdot\mathbf{S}$) and antisymmetric ($\mathbf{S}\times\mathbf{S}$) exchange interactions (see Methods):

$$\begin{aligned}\mathcal{H}_0 = &\sum_{i,j}^{\mu=1} J_1\left(s_{ix}s_{jx} + s_{iy}s_{jy} + \Delta s_{iz}s_{jz}\right)\\ &+ \sum_{i,j}^{\mu=2,\ldots,7} J_\mu \mathbf{s}_i\cdot\mathbf{s}_j + \sum_{i,j}^{\mu=4} \mathbf{D}_4\cdot\left(\mathbf{s}_i\times\mathbf{s}_j\right)\\ &- \sum_{i,j}^{\mu=3,4} B_{\mathrm{biq}}\left(\mathbf{s}_i\cdot\mathbf{s}_j\right)^2,\end{aligned} \tag{1}$$

where $\mathbf{s}_i$ is the classical spin vector, the length of which is normalized to be unity ($|\mathbf{s}_i| = 1$). We adopt the same definitions of bond numbers for the exchange integrals (J_μ ($\mu = 1$–7) than in ref. [14]. We used model parameters evaluated in [13] after renormalizing them such that the norm of classical spin vector $\mathbf{s}_i$ becomes unity and slight tuning so as to reproduce the two experimentally measured temperatures of magnetic transitions. The parameters used for the calculations are listed in Supplementary Table 1.

Figure 4a shows a theoretical phase diagram of CuO as a function of temperature, which is built according to the specific heat and the spin helicity vector calculated by the Monte–Carlo simulations. The specific heat in Fig. 4b exhibits two peaks associated with the successive magnetic phase transitions, i.e., the transition from PM to AF2 phases at 230 K and the subsequent transition from AF2 to AF1 phases at 213 K. The spin helicity vector $\mathbf{h}$ in Fig. 4c exhibits a relatively large component $h_{[\bar{1}01]}$ in the AF2 phase, whereas it is abruptly reduced at the phase transition to the AF1 phase. This result indicates that the expected spiral order with rotating spins is stabilized for the AF2 phase, whereas the expected nearly collinear order with slightly canted spins is stabilized for the AF1 phase. Unlike the previous theoretical model[14], our model accounts for the complex phase diagram of CuO, providing quantitatively precise critical temperatures. This effective spin model enables us to calculate absorbance spectra due to magnetoelectric excitations in the THz range.

The absorbance spectra $\alpha(\omega)$ is calculated from dynamical dielectric susceptibility $\varepsilon(\omega)$ as,

$$\alpha(\omega) \propto \omega \mathrm{Im}[\varepsilon(\omega)]. \tag{2}$$

To determine $\varepsilon(\omega)$, we assume the antisymmetric exchange model for the spin-dependent electric polarizations $\mathbf{p}_{ij} \propto \mathbf{e}_{ij}\times(\mathbf{s}_i\times\mathbf{s}_j)$ on the bonds associated with J_3 and J_4 (Methods). The absorbance spectra for the AF2 phase at $T = 216$ K and the AF1 phase at T = 200 K in the THz range are presented in Fig. 4d for an in-plane light polarization $\mathbf{E}^{\omega}\|[101]$. We also have calculated the absorption spectra for the in-plane perpendicular configuration $\mathbf{E}^{\omega}\|[10\bar{1}]$ (dotted curve of Fig. 4d) and the out-of-plane perpendicular configuration $\mathbf{E}^{\omega}\|[010]$ (supplementary Fig. 5). As expected, the excitations are silent in the $\mathbf{E}^{\omega}\|[10\bar{1}]$ channel. However, in the $\mathbf{E}^{\omega}\|[010]$ channel the result of numerical simulations shows a spectral response of the electromagnons in the AF2 phase. This is in contradiction with our experimental measurements presented in supplementary Fig. 1, as well as with previous works[13,14]. This result demonstrates that our effective hamiltonian model does not allow to fully recover the complex physics of the electromagnons

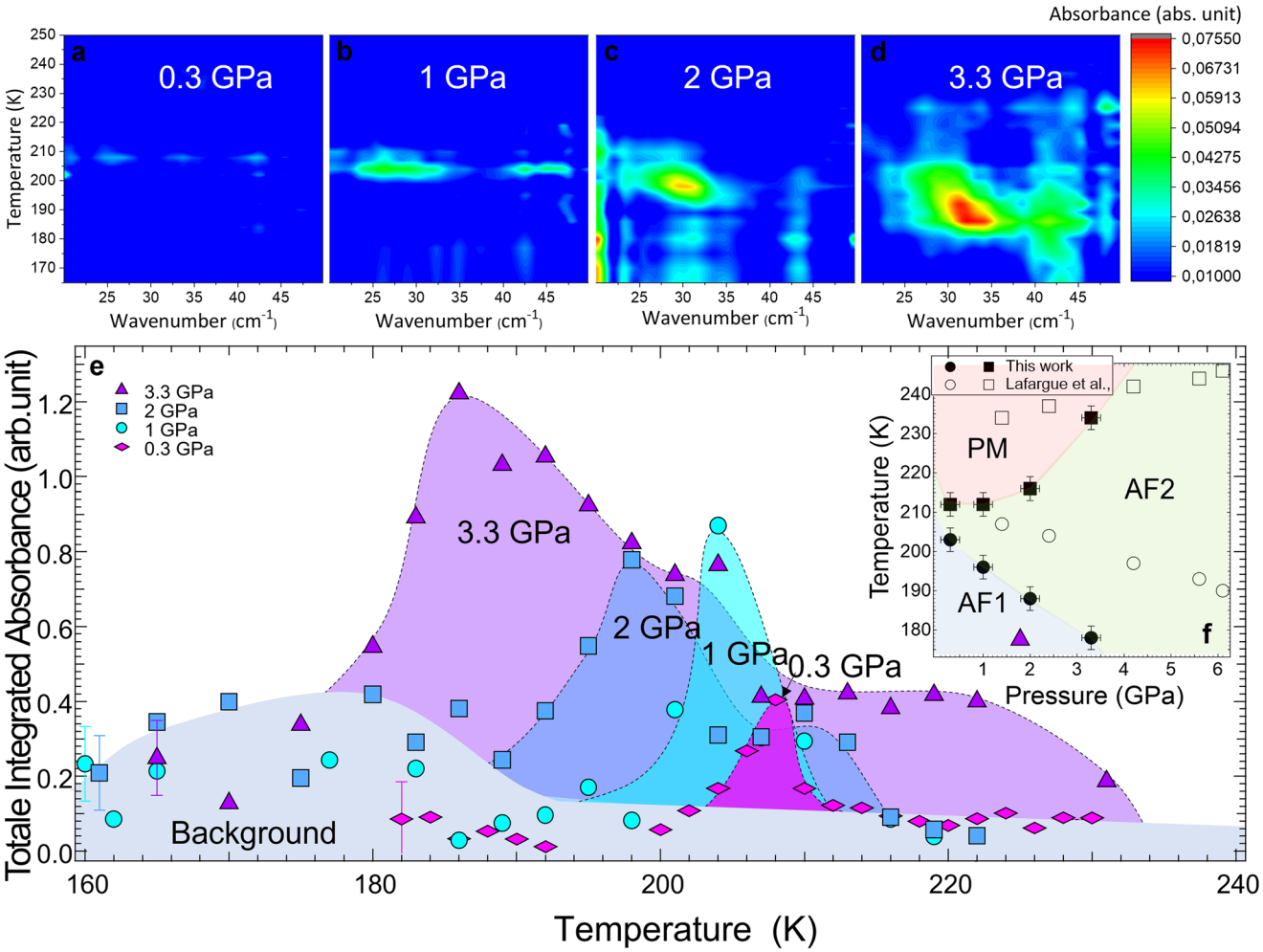

Fig. 3 Pressure dependence of the integrated electromagnon absorbance as a function of temperature. a–d 2D colormap of the integrated absorbance (color scale) as a function of wavenumber (*x*) and temperature (*y*). **e** Total integrated absorbance extracted between 20 and 50 cm^{-1} (0.6–1.5 THz) as a function of temperature for each value of pressure. The background (see Methods) represented in gray is evaluated from the contribution of the other 2 excitations (EX1 and EX2). y error bars are represented for the low-temperature point for each value of pressure and are equal to ±0.1 (background value of the total integrated absorbance). **f** P-T phase diagram of CuO obtained from our THz spectroscopy determination of the temperature range of existence of the EM electromagnon compared to the previous dielectric constant measurements from Lafargue et al.[7]. The *x* and *y* error bars are estimated from the temperature and pressure experimental determination and are equal to ±0.2 GPa and ±3 K for *x* error bar and *y* error bar, respectively.

in CuO. For now, we have no explanation for this discrepancy. Anyway, for lack of anything better, and as it allows to recover quantitatively the phase diagram of CuO and the absorption spectra for the ac-plane channels ($\mathbf{E}^{\omega}$ in the ac-plane), we consider our effective hamiltonian spin-model to be valid to explain properties of CuO in the ac-plane where the antiferromagnetic interactions are the strongest. The seek for a better model goes beyond the scope of this work which remains mainly experimental but is worth to be addressed in future theoretical works which could also lead to better understanding of the origin of the EX1 end EX2 excitations.

DISCUSSIONS

The inset of Fig. 3 compares the P-T phase diagram associated with the T_{N1} and T_{N2} we obtained from the existing range of the EM electromagnon and the transition temperatures of the multiferroic phase based on dielectric constant measurements under pressure recently reported[7]. Both measurements are compatible with an expansion of the multiferroic phase under high pressure. However, there is a difference that can be seen as a systematic shift of ~20 K in the temperature values. In the work of Lafargue-Dit-Hauret et al.[7] the temperatures of the AF2 phase are determined by the edge of the peaks of the dielectric constant whereas in our measurements the phase diagram is based on the temperature appearance of the EM electromagnon. Moreover as discussed before, the positions of the temperature sensors in both experiments are not the same. In our case, the temperature sensor is attached to the DAC. This might explain the discrepancy in the absolute value of temperature between the two experiments.

The comparison between the experimental absorbance spectrum of Fig. 1a at ambient pressure and the calculated one of Fig. 4d at $T = 216$ K (AF2 phase) are in qualitative agreement. More specifically, the calculated spectrum in the AF2 phase reproduces well the three spectral peaks of EM, EX1, and EX2 with respect to the wave numbers and the intensity ratios. On the other hand, the calculated spectrum for the AF1 phase also exhibits broad peaks which correspond to the EM, EX1, and EX2 excitations, although the intensities are significantly suppressed as compared to those for the AF2 phase. In addition, another low-energy excitation shows up ~16.5 cm^{-1} (0.5 THz). This excitation is indeed visible in the experimental spectra in Fig. 1a (arrow).

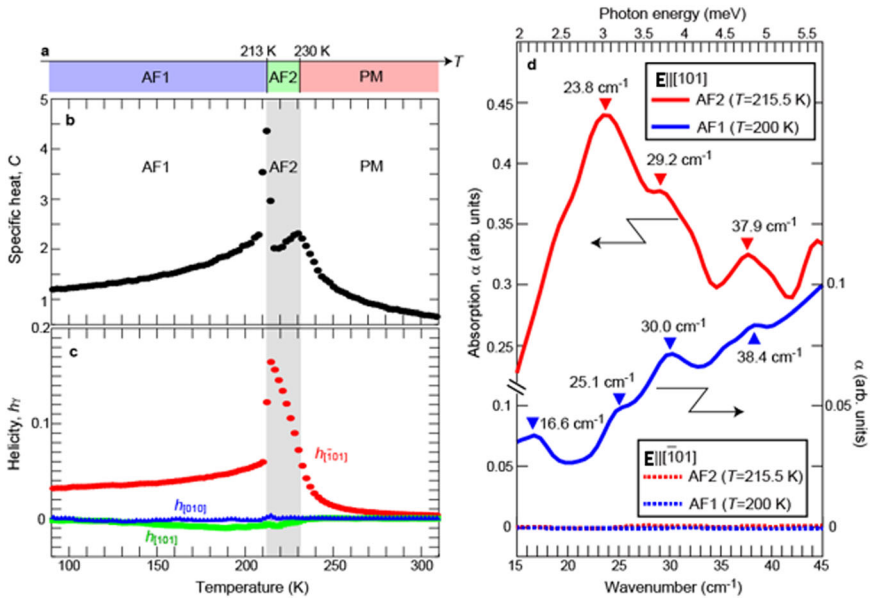

Fig. 4 Theoretical magnetic phase diagram and simulated absorbance response of the electromagnons in the THz energy range. **a** Theoretical phase diagram of CuO as a function of temperature. **b** Temperature profile of specific heat *C*. **c** Temperature profiles of the components of spin helicity vector $h_{[\bar{1}01]} \equiv \mathbf{h} \cdot \mathbf{E}_{[\bar{1}01]}$, $h_{[101]} \equiv \mathbf{h} \cdot \mathbf{e}_{[101]}$, and $h_{[010]} \equiv \mathbf{h} \cdot \mathbf{e}_{[010]}$, where $\mathbf{e}_{[\bar{1}01]}$, $\mathbf{e}_{[101]}$ and $\mathbf{e}_{[010]}$ are unit directional vectors in respective directions. **d** Absorbance spectra $\alpha(\omega)$ for the AF2 phase ($T = 216$ K) and the AF1 phase ($T = 200$ K) for two in-plane light polarizations $\mathbf{E}^{\omega} \| [101]$ and $\mathbf{E}^{\omega} \| [\bar{1}01]$. The spectra are calculated by assuming the antisymmetric exchange-striction mechanism ($\mathbf{S} \times \mathbf{S}$ mechanism) for the spin-dependent electric polarizations.

It is worth mentioning that the temperature profiles of spin helicity in Fig. 4c clearly show a sharp anomaly (jump) at the AF1-to-AF2 phase transition point, which explains the sudden increase of spectral intensity of the electromagnon excitation (EM) at the transition point and its gradual disappearance with increasing temperature. Moreover, we can see that unlike the components of other directions ($h_{[010]}$ and $h_{[101]}$), the component of $[\bar{1}01]$ direction, i.e., $h_{[\bar{1}01]}$ never goes to zero and increases gradually as temperature increases in the AF1 phase. The calculations show a small but finite spin helicity $h_{[\bar{1}01]}$ even in the AF1 phase, where the spins are aligned in a nearly collinear manner but are slightly canted to form an elliptically deformed spiral. In this configuration, the $\mathbf{S} \times \mathbf{S}$ mechanism is activated and enables the existence of electromagnons even in the AF1 phase. From the numerical results, we can say that there is a magnetic phase transition associated with the spin helicity but we cannot distinguish a finite helicity and a fluctuating helicity (they give the same contribution in the Monte-Carlo simulations). In the experimental results however, EX1 and EX2 excitations have an increasing spectral weight in AF1 phase (cf Fig. 2) suggesting a nonzero spin helicity in this phase and thus a possible existence of ferroelectricity. Up to now, no ferroelectricity has been reported in the AF1 phase. This might be due to: (i) a particular magnetic structure that leads to compensation of polarization at long range (no macroscopic polarization); (ii) a value of polarization that is very small because of a tiny helicity that cannot be detected up to now by experiments.

It should also be mentioned that there are neither magnetic resonances active to the light magnetic field $\mathbf{H}^{\omega}$ nor electromagnons of $\mathbf{S} \cdot \mathbf{S}$ origin in the present frequency regime, and the three excitations observed are all attributable to the electromagnons of $\mathbf{S} \times \mathbf{S}$ origin (Eq. (1)).

The prospects of this work are not limited to bringing the electromagnon to room temperature at a pressure of ~10 GPa, but we can also expect to considerably enhance its electric-dipole activity. However such pressures remain a laboratory adjustment button. In order to enable CuO electromagnon to reach its potential application, both of these properties must be found in thin films and even more in thin films on substrates relevant to the semiconductor industry. CuO films deposited on Si are already used in solar cells[15] or capacitors[16], for example. Interestingly, the most common and stable phase of CuO in the form of thin films is the monoclinic crystal lattice and preliminary studies suggest that CuO films possess a multiferroic phase and in particular under strain[17]. This point is even more encouraging since the hydrostatic pressure could be replaced by misfit strain engineering in CuO thin films although the two are not equivalent. From the elastic constants of CuO[18], we roughly estimated that a pressure of 3 GPa could be reached in two dimensions with a misfit of 4–5%. CuO thin films on silicon have a good sense to have a misfit strain of ~5% which would fulfill the necessary conditions for an increase of the electromagnon properties of CuO towards the ambient temperature. CuO on GaAs should make it possible to reach a strain of ~8%. $SrTiO_3$ substrate could further allow obtaining a multiferroic phase and a strong electric-dipole activity of the electromagnon at room temperature although the strains induced by a misfit of about 25% will relax to form dislocations. The systematic study of the strain effect on CuO thin films will shed light on this question.

In conclusion, thanks to the high brilliance and high resolution of the THz beam exploited at the AILES beamline of synchrotron SOLEIL, we were able to identify and track three electromagnons in CuO compounds in the THz range. When hydrostatic pressure is applied, the strength of the characteristic electromagnon of the CuO multiferroic phase is multiplied by almost an order of magnitude. Simultaneously, the existing temperature range of this electromagnon increases by more than 40 K, showing a promising perspective for room temperature electromagnons. In addition, we propose a classical Heisenberg model which, combined with Monte-Carlo numerical simulations and spin-dynamics, reproduced quantitatively the magnetic phase diagram of CuO. Our numerical simulations also allow obtaining THz absorbance spectra at zero pressure. Even if our model does not allow us to fully recover the complex physics of CuO it is in good agreement with our experimental results in the plane where the magnetic interactions are the strongest, namely the ac-plane. Although

further theoretical work would be needed, our hamiltonian model certainly constitutes a first step for the theoretical modeling of the complex physics of CuO. Finally, by demonstrating the increase of both the resilience and existence temperature range of the electromagnons under pressure, this work places CuO on the horizon of the spin wave-based technology roadmap and paves the way towards engineered electromagnon under epitaxial strain in dedicated CuO thin films.

METHODS

Samples

The CuO single crystals used in this work were synthesized using the flux technique starting from CuO (Alfa Aesar, powder, 99,99%) and using PbO (Alfa aesar, powder, 99.9%) as a flux in (70:30) molar ratio. The powders were mixed by grinding in agate mortar. The mixture was placed in a platinum crucible and heated to 1100 °C in a standard muffle furnace under air, and dwelled for 4h to ensure total homogeneous melting. The temperature was then slowly decreased to 850 °C (PbO melting point) at a rate of 0.5 °/h before fast cooling down to room temperature. This method allowed the obtention of high-quality single crystals of typically (2 mm × 1 mm × 1 mm)-size. Powder X-ray diffraction on grinded single crystals confirmed the phase purity and magnetic measurements confirmed the occurrence of the expected two magnetic transitions at $T_{N1} = 213$ K and $T_{N2} = 230$ K. Crystals were then cutted along the ac-plane using a Leica diamond wire saw and the [101] direction was determined using a Rigaki Xcalibur S 4-circles xrd diffractometer. For temperature measurement outside the DAC, a thick sample of 3 mm × 2 mm × 1 mm was used (sample named 0P-CuO). For high-pressure measurement, the CuO sample (sample named HP-CuO) thickness have been reduced to 500 µm × 400 µm × 60 µm using a Leica mechanical micropolisher.

Spectroscopy

Infrared spectroscopy measurements in the THz range were performed in the transmission configuration on an IFS125MR Michelson interferometer exploiting the synchrotron radiation extracted on the AILES beamline of synchrotron SOLEIL[19]. A 50 µm Mylar beamsplitter and a 1.6 K pumped-bolometer were used to perform the measurements in the THz range between 15 and 50 cm^{-1} (0.6–1.5 THz) with a resolution of 0.5 cm^{-1} (0.015 THz). Due to the extraction process the Electric field of incident synchrotron radiation ($\mathbf{E}^{\omega}$) is naturally linearly polarized vertically in this energy range.

Measurements as a function of temperature and without applied pressure were performed in transmission configuration between room temperature and 15 K using a helium close-cycle cryostat. High-pressure measurements were realized as a function of temperature in transmission mode inside a DAC connected to a cold tip of an open-cycle He-cryostat and placed in the focus point of two highly focusing optics[20]. The optical setup allows a strong focusing and a quasi-normal incidence of the synchrotron beam onto the sample surface. The diameter of the culets of the diamond anvil was 1mm. A rhenium gasket preindented and then drilled allowed to get a 500 µm diameter and 100 µm thick hole adapted to the sample size. Polyethylene (PE) powder was used as a transmitting medium to fill the hole and 2 ruby balls were placed next to the sample to allow in-situ determination of the pressure using fluorescence.

The references used for the calculation of the absorbance spectra presented above are the transmission spectra of the sample itself in the same condition of pressure and alignment but at 250 K, in the paramagnetic phase, where no excitation exists in the THz range. The presented absorbance spectra as a function of temperature and pressure obtained inside the DAC were treated using an Igor pro adapted procedure for suppressing the interference fringes[21,22] and then smoothed over 20 points using the Igor Pro data treatment software.

In Fig. 3, we have chosen to treat as a background all the contributions to the total area that are not due to the EM excitation. As discussed in the text, EM is predominant in the AF2 phase and we estimate its appearance/disappearance at the point where the absolute derivative of the curve is maximum. This background contribution is mainly due to the presence of the EX1 and EX2 excitations that are stronger at low temperatures and reinforced under high pressure which justifies the shape of the background we have chosen.

Numerical calculations

The electromagnon absorbance spectra in CuO at finite temperatures are calculated by using a classical Heisenberg model given in Eq. (1), which can reproduce the experimentally observed successive phase transitions and two transition temperatures at quantitative level. The first and second terms of the Hamiltonian represent the symmetric exchange interactions. We consider seven kinds of exchange couplings J_μ ($\mu = 1$–7) on different crystallographic bonds according to ref. [14]. To reproduce the collinear spins oriented nearly along the b-axis in AF1 phase, we introduce a tiny XXZ-type anisotropy Δ. Note that CuO is the spin-1/2 system in which the quadratic-type spin anisotropy like $K\sum_i s_{iz}^2$ must be vanished. The third term represents the Dzyaloshinskii–Moriya interaction on the bonds of J_4. The fourth term represents biquadratic interactions for the bonds of J_3 and J_4, which favors collinear alignment of the two spins connected by the bonds. For the parameters, we use the values listed in Supplementary Table 1. This set of parameters reproduces the experimentally observed two magnetic transition temperatures $T_{N1} = 213$ K and $T_{N2} = 230$ K of successive magnetic transitions.

The temperature profiles of specific heat C and spin helicity $\mathbf{h}$ are calculated by the Monte-Carlo simulation using the following formulas,

$$C = \frac{\langle E^2 \rangle - \langle E \rangle^2}{N(k_B T)^2}, \tag{3}$$

$$\mathbf{h} = \left\langle \frac{1}{N}\sum_{i=1}^{N} \mathbf{s}_i \times \left(\mathbf{s}_{i+\hat{a}+\hat{b}/2} + \mathbf{s}_{i+\hat{a}-\hat{b}/2} + \mathbf{s}_{i+\hat{c}+\hat{b}/2} + \mathbf{s}_{i+\hat{c}-\hat{b}/2} \right) \right\rangle, \tag{4}$$

where N is the number of Cu sites.

To calculate the absorbance spectra at a specified temperature, we first prepare N_s(=100) spin configurations of thermal equilibrium at the temperature using Monte–Carlo thermalization. Then we simulate the spin dynamics after applying a light pulse to each spin configuration using the time-evolution equation of spins,

$$\hbar \frac{d\mathbf{s}_i}{dt} = -\mathbf{s}_i \times \mathbf{H}_i^{\mathrm{eff}}. \tag{5}$$

Here the effective magnetic field $\mathbf{H}_i^{\mathrm{eff}}$ acting on the spin $\mathbf{s}_i$ is given by,

$$\mathbf{H}_i^{\mathrm{eff}} = -\frac{\partial \mathcal{H}}{\partial \mathbf{m}_i}. \tag{6}$$

We solve this equation numerically using the fourth-order Runge–Kutta method. For the coupling to the light electric field, we add the following terms to the Hamiltonian,

$$\mathcal{H}_E = -\mathbf{E}^{\omega}(t) \cdot \sum_i \mathbf{p}_i. \tag{7}$$

This term $\mathcal{H}_E$ represents the coupling between the time-dependent electric field $\mathbf{E}^{\omega}(t)$ and the local electric polarizations $\mathbf{p}_i$. We assume the antisymmetric exchange-striction mechanism

($\mathbf{S}\times\mathbf{S}$ mechanism) for the spin-induced electric polarizations, where the local electric polarization $\mathbf{p}_i$ is given by,

$$\begin{aligned}\mathbf{p}_i = \lambda\Big[&\mathbf{e}_{\hat{c}+\hat{b}/2}\times\left(\mathbf{s}_i\times\mathbf{s}_{i+\hat{c}+\hat{b}/2}\right)\\ &+\mathbf{e}_{\hat{c}-\hat{b}/2}\times\left(\mathbf{s}_i\times\mathbf{s}_{i+\hat{c}-\hat{b}/2}\right)\\ &+\mathbf{e}_{\hat{a}+\hat{b}/2}\times\left(\mathbf{s}_i\times\mathbf{s}_{i+\hat{a}+\hat{b}/2}\right)\\ &+\mathbf{e}_{\hat{a}-\hat{b}/2}\times\left(\mathbf{s}_i\times\mathbf{s}_{i+\hat{a}-\hat{b}/2}\right)\Big].\end{aligned} \tag{8}$$

Here λ is the magnetoelectric coefficient. We assume the following form of the pulse,

$$\mathbf{E}^{\omega}(t) = \begin{cases} E^{\omega}\mathbf{e}_{\gamma} & 0\le t\le 1\\ 0 & t>1\end{cases} \tag{9}$$

where γ is an index that specifies the light polarization. We simulate the time profile of $\Delta P_{\gamma}(t)\equiv P_{\gamma}(t)-P_{\gamma}(0)$ after the application of the electric-field pulse $\mathbf{E}^{\omega}(t)$ for each spin configuration. Here $P_{\gamma}(t)$ is the net polarization, which is given by,

$$P_{\gamma}(t) = \frac{1}{N}\sum_i p_{i\gamma}(t). \tag{10}$$

We take the average $\Delta\langle P_{\gamma}(t)\rangle_{\mathrm{av}}$ over the N_s spin configurations and calculate the Fourier coefficient to obtain the dynamical dielectric susceptibility $\varepsilon_{\gamma}(\omega)\propto\langle\Delta P_{\gamma}(\omega)\rangle_{\mathrm{av}}$. The absorbance spectra $\alpha(\omega)$ is obtained by $\alpha_{\gamma}(\omega)\propto\omega\mathrm{Im}[\varepsilon_{\gamma}(\omega)]$.

DATA AVAILABILITY

The authors declare that data supporting the findings of this study are available from the corresponding author M.V. upon request.

Received: 13 May 2022; Accepted: 9 February 2023;
Published online: 24 February 2023

REFERENCES

1. Chumak, A. V., Serga, A. A. & Hillebrands, B. Magnonic crystals for data processing. *J. Phys. D: Appl. Phys.* **50**, 244001 (2017).
2. Rezende, S. M. Fundamentals of magnonics. *lecture Notes in Physics*, 1st ed., **969** (Springer, 2020).
3. Barman, A. et al. The 2021 magnonics roadmap. *J. Phys.: Condens. Matter* **33**, 413001 (2021).
4. Shen, R.-C. et al. Long-Time memory and ternary logic gate using a multistable cavity magnonic system. *Phys. Rev. Lett.* **127**, 183202 (2021).
5. Schoenherr, P. et al. Local electric-field control of multiferroic spin-spiral domains in $TbMnO_3$. *npj Quantum Mater.* **5**, 86 (2020).
6. Rocquefelte, X., Schwarz, K., Blaha, P., Kumar, S. & van den Brink, J. Room-temperature spin-spiral multiferroicity in high-pressure cupric oxide. *Nat. Commun.* **4**, 2511 (2013).
7. Lafargue-Dit-Hauret, W. et al. Potential room-temperature multiferroicity in cupric oxide under high pressure. *Phys. Rev. B* **103**, 214432 (2021).
8. Mostovoy, M. Multiferroics go high-T_C. *Nat. Mater.* **7**, 269–270 (2008).
9. Kimura, T., Sekio, Y., Nakamura, H., Siegrist, T. & Ramirez, A. P. Cupric oxide as an induced-multiferroic with high-T_C. *Nat. Mater.* **7**, 291–294 (2008).
10. Forsyth, J. B., Brown, P. J. & Wanklyn, B. M. Magnetism in cupric oxide. *J. Phys. C: Solid State Phys.* **21**, 2917–2929 (1988).
11. Brown, P. J., Chattopadhyay, T., Forsyth, J. B. & Nunez, V. Antiferromagnetism in CuO studied by neutron polarimetry. *J. Phys.: Condens. Matter* **3**, 4281–4287 (1991).
12. Ain, M., Menelle, A., Wanklyn, B. M. & Bertaut, E. F. Magnetic structure of CuO by neutron diffraction with polarization analysis. *J. Phys.: Condens. Matter* **4**, 5327–5337 (1992).
13. Jones, S. P. P. et al. High-temperature electromagnons in the magnetically induced multiferroic cupric oxide driven by intersublattice exchange. *Nat. Commun.* **5**, 3787 (2014).
14. Cao, K., Giustino, F. & Radaelli, P. G. Theory of electromagnons in CuO. *Phys. Rev. Lett.* **114**, 197201 (2015).
15. Dolai, S. et al. Cupric oxide (CuO) thin films prepared by reactive dc magnetron sputtering technique for photovoltaic application. *J. Alloy. Compd.* **724**, 456 (2017).
16. Hilman, J., Yost, A. J., Tang, J., Leonard, B. & Chien, T. Low temperature growth of CuO nanowires through direct oxidation. *Nano-Struct. Nano-Objects* **11**, 124 (2017).
17. Goswami, S. et al. Large magnetoelectric coupling in the thin film of multiferroic CuO. *ACS Omega* **5**, 22890 (2020).
18. Yao, B. et al. First-principles calculations on phase transformation and elastic properties of CuO under pressure. *J. Comput. Electron.* **17**, 1450 (2018).
19. Roy, P., Rouzières, M., Qi, Z. & Chubar, O. The AILES infrared beamline on the third generation synchrotron radiation facility SOLEIL. *Infrared Phys. Technol.* **49**, 139–146 (2006).
20. Voute, A. et al. New high-pressure/low-temperature set-up available at the AILES beamline. *Vib. Spectrosc.* **86**, 17–23 (2016).
21. Faggin, M. F. & Hines, M. A. Improved algorithm for the suppression of interference fringe in absorption spectroscopy. *Rev. Sci. Instrum.* **75**, 4547–4553 (2004).
22. Aupiais, I. et al. Colossal electromagnon excitation in the non-cycloidal phase of $TbMnO_3$ under pressure. *npj Quantum Mater.* **3**, 60 (2018).

ACKNOWLEDGEMENTS

The authors would like to thank B. Baptiste of the DRX platform of the IMPMC laboratory (Sorbonne University) for the orientation of the samples before the experiment, M. Lheronde of the IPANEMA-CNRS platform for the availability of their surface preparation laboratory. The authors thank the synchrotron SOLEIL for the provision of beamtime (proposal No. 20190590 and 20201412). M.M. and T.I. are supported by JSPS KAKENHI (Grant No. 20H00337), CREST, the Japan Science and Technology Agency (Grant No. JPMJCR20T1), and Waseda University Grant for Special Research Projects (Project No. 2021C-566).

AUTHOR CONTRIBUTIONS

The samples were grown by D.B. and D.C.; M.V., P.H., J-B.B., P.R., and M.C. performed experiments and analyzed the data; T.I. and M.M. developed the model and performed the simulations. All authors discussed the results and wrote the manuscript.

COMPETING INTERESTS

The authors declare no competing interests.

ADDITIONAL INFORMATION

Supplementary information The online version contains supplementary material available at https://doi.org/10.1038/s41535-023-00542-1.

Correspondence and requests for materials should be addressed to M. Verseils.